





Unified scaling law for wall friction in laterally confined flows of shape anisotropic particles

Antonio Pol , Riccardo Artoni *, and Patrick Richard 
GPEM, MAST, Université Gustave Eiffel, 44344 Bouguenais, France

 (Received 9 November 2022; accepted 18 July 2023; published 14 August 2023)

In this work we discuss a scaling law for wall friction weakening in three-dimensional, dense, fully confined granular flows made of shape anisotropic particles. Using particle-based simulations, we observe a rich variety of kinematics and wall stress profiles by varying the particle-wall friction coefficient and the cell width. We show that in this peculiar flow configuration: (i) particle shape has a negligible influence on translational velocity and granular temperature profiles while the angular motion is strongly hampered for elongated particles and (ii) the mobilization of friction at the sidewalls is affected by both particle shape and flow pattern. Associating data on wall stress and particles kinematics, we find that wall friction mobilization is well described by a scaling law based on a balance between sliding and rolling motion of the grains. We show that the proposed scaling law seems to be very robust, being independent of the main system parameters, e.g., particle-particle friction, particle-wall friction, channel width, vertical confinement, particle elongation, and flow configuration (shear driven or gravity driven). This result highlights the importance of angular motion of the particles for the understanding of the behavior at flat boundaries and may reignite the debate about the relevant variables in theories for dense granular flows.

DOI: [10.1103/PhysRevFluids.8.084302](https://doi.org/10.1103/PhysRevFluids.8.084302)

I. INTRODUCTION

The interaction of flowing granular media with flat frictional interfaces is extremely frequent both in geophysical phenomena (e.g., flows in canyons and grain transport in channels) and in industrial applications (e.g., silos, hoppers, and mixers). These interfaces may introduce nonlocal effects that strongly affect the flow properties over distances of the order of several grain diameters [1,2]. Moreover, high flow heterogeneity may develop with the coexistence of static, creeplike, and shear localization regions [3]. The understanding of the behavior at interfaces is therefore a preeminent scientific challenge and is fundamental for a full three-dimensional (3D) rheological model of granular flows. In terms of continuum modeling, walls are interfaces to which appropriate boundary conditions have to be assigned. Such boundary conditions therefore have to take into account the phenomenology of the interaction between the granular material and the wall and have to consider at least the wall forces (wall friction) and velocities (wall slip). Previous works have shed light on the collective particle-wall interaction, by highlighting the existence of wall friction weakening [3–5], which is related to the incomplete mobilization of friction in slowly moving zones. Boundary conditions in the form of scaling laws for effective wall friction have also been discussed, invoking different weakening mechanisms, associated with either velocity fluctuations or particle angular motion. In Refs. [3,6] the ratio $v_x/\sqrt{T_x}$ (where v_x is the streamwise average sliding velocity and T_x represents the streamwise velocity fluctuations) was used to define a scaling law for the

*riccardo.artoni@univ-eiffel.fr

effective friction at smooth interfaces, thus associating the weakening of the effective friction with the random oscillatory motion of the particles in the flow direction. Differently, in Ref. [7] the degradation of wall friction was related to a rotational index based on the relative importance of rotation-induced and sliding velocity. Those scalings showed fair agreement with the data, but they were only applied to the case of spherical particles. Recently, Pol *et al.* showed that the balance between sliding and angular motion at the wall is affected by particle shape [8], and therefore one may speculate that the wall friction weakening mechanisms can also be affected by particle anisotropy.

In this paper we study, by means of an extensive campaign of discrete element simulations, the effective friction at lateral flat frictional walls in a fully confined and shear-driven dense granular flow composed of shape anisotropic particles. Such a numerical setup and its experimental counterpart have proven to be useful in the past to finely characterize wall friction weakening in confined flows of spherical particles [3,5,6,9,10]. We show that wall stresses, and thus effective wall friction, are affected by particle shape through both the average and the fluctuating components of the angular motion. This indicates that the angular dynamics is a crucial mechanism and supports the idea that particle rotations should be included in theories aiming to describe the behavior of dense granular flows in the vicinity of an interface. We first briefly describe the numerical method in Sec. II and then analyze the translational and rotational kinematics of the particles in Sec. III. In Sec. IV we show how wall friction weakening is affected by the particle shape and deduce an alternative scaling law for lateral wall friction, which is verified against a gravity-driven confined flow configuration. Finally, a summary, conclusions, and perspectives for future work are presented in Sec. V.

II. NUMERICAL SIMULATIONS

Using the open-source molecular-dynamics code LIGGGHTS [11], we perform 3D discrete element simulations of dense and fully confined granular flows. The flow configuration (Fig. 1) is a rectangular cuboid ($L_x = 20a$ and $L_y = 10d$, with a and d the maximum and the minimum axis of a particle, respectively, and L_z the variable height) with periodic boundary conditions in the flow direction, i.e., x direction. The flow is confined by two flat but frictional sidewalls and by a top and a bottom bumpy wall (regular triangular mesh of spheres of diameter d with a spacing of $1.5d$) vertically. The flow is driven by the motion of the bottom wall at a fixed velocity V and the system is submitted to gravity g . In the following we call x the flow (streamwise) direction, y the direction normal to the sidewalls, and z the transverse (vertical) direction. The top wall is fixed in the x and y directions but can freely move in the z direction according to the balance between its weight

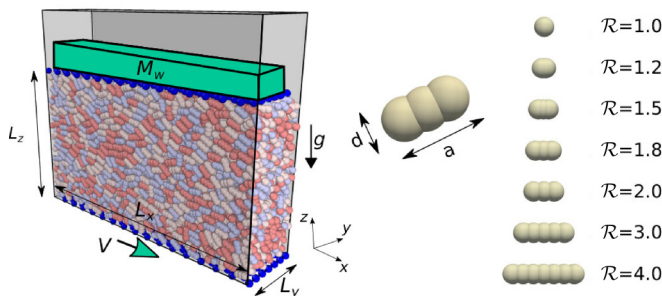


FIG. 1. Typical geometry of the discrete element simulations and of the particle shapes characterized by their aspect ratio $\mathcal{R} = a/d$. The flow configuration is a shear cell made of a bumpy bottom (dimensions $L_x \times L_y$), a bumpy top, and two sidewalls separated by a gap L_y . The shear is ensured by the bumpy bottom, which moves at a constant velocity V in the x direction. The top flow is a bumpy horizontal wall submitted to a force $M_w g$.

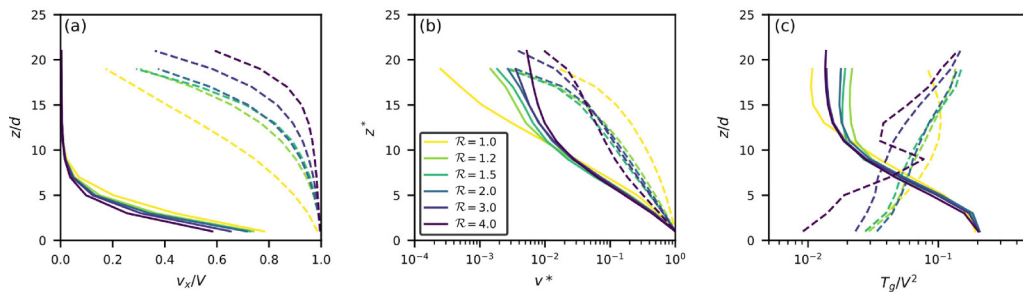


FIG. 2. Vertical profiles of (a) translational velocity v_x , (b) rescaled velocity v^* , and (c) granular temperature T_g . Cases characterized by $\mu_{pw} = 0.3$ ($\mu_{pw} = 0.05$) are represented with a solid (dashed) line. The legend in (b) applies to all figures.

$M_w g$ and the force exerted by the grains. The bottom wall velocity and top wall mass are made dimensionless by considering $\tilde{V} = V/\sqrt{gd}$ and the ratio of the wall mass over the total mass of the grains $\tilde{M} = M_w/M_g$, respectively. Simulations are carried out with $N \sim 4000$ – 5000 particles with diameter d and a variable length to diameter (aspect) ratio $\mathcal{R} = a/d$ ($1.2 \leq \mathcal{R} \leq 4$). In this context, clumps of spheres with an overlap of $d/2$ (overlap is larger for $\mathcal{R} < 2$) and $\pm 5\%$ radius variation are used (Fig. 1). Preliminary analyses show that larger overlaps between the clump's members give equivalent results. Spheres ($\mathcal{R} = 1$) are also considered for comparison with the shape isotropic case. Particle density is set equal to $\rho = 6/\pi$ in order to have a unitary mass for spherical particles.

The particles' interaction is ruled by a spring-dashpot model in the normal direction $F_n = k_n \delta_n - \gamma_n \dot{\delta}_n$, with k_n and γ_n the stiffness of the spring and the viscosity of the dashpot, respectively, δ_n the overlap, and $\dot{\delta}_n$ the normal component of the relative velocity of the particles. The stiffness k_n is taken equal to $5 \times 10^6 mg/d$ (with m the mass of a spherical particle) and γ_n is set in order to have a normal restitution coefficient of 0.7. The adopted value of k_n ensures having deformations much lower than the grain size. From a simple dimensional analysis one can estimate that the pressure acting on a grain located at the bottom of the cell is $P^* \sim \rho g L_z (\tilde{M} + 1)$ and therefore the grain's deformation is of the order of $P^* d/k_n$ (approximately 5×10^{-5} , with $\tilde{M} = 4.8$, which is the largest value used in this study). In the simulations, the grains' overlap may be slightly larger than our estimated value due to dynamics effects; however, this is always below approximately $5 \times 10^{-4} d$. The tangential force is ruled by a spring model ($F_t = k_t \delta_t$ and $k_t = 2k_n/7$) and the deformation δ_t (i.e., elastic tangential displacement between the particles) is limited by a Coulomb plastic condition with a friction coefficient μ_{pp} . The contact between a particle and the sidewalls is treated in the same manner but with a friction coefficient μ_{pw} . The time step adopted in the numerical simulations is $dt = 2 \times 10^{-5} \sqrt{d/g}$, which corresponds to $\frac{1}{50}$ of the typical collision duration.

In the remainder of the paper $\tilde{V} = 1$, $\tilde{M} = 1.2$, and $\mu_{pp} = 0.3$ are used, unless specified otherwise. In order for the material to lose memory of the initial structure, the medium is allowed to flow during a time Δt until reaching a minimal local shear deformation $\gamma = \dot{\gamma}(z)\Delta t > 5$ [$\dot{\gamma}(z) = \partial v_x / \partial z$], which ensures reaching a stationary state [12]. In this paper, unless stated otherwise, we present average quantities computed by performing time averages on slices of thickness $2d$ in the z direction and considering only the particles that are interacting with the sidewalls (vertical regions characterized by $y \leq 1.05 \frac{d}{2}$ and $y \geq L_y - \frac{d}{2}$). This choice is motivated by the fact that the scaling laws for the boundary behavior are expected to hold locally at the wall.

III. KINEMATICS

A. Particle shape: Aspect ratio \mathcal{R}

Translational velocity profiles obtained for different aspect ratios and two values of the particle-wall friction coefficient $\mu_{pw} = 0.05$ (dashed line) and $\mu_{pw} = 0.3$ (solid line) are shown in Fig. 2(a).

The flow displays a clear shear localization, the flow regime being strongly affected by the wall friction: As previously observed for spheres [3], shear localizes in the bottom region of the flow for the larger value of μ_{pw} , while it localizes near the top wall for the lower μ_{pw} value. In both cases, an exponential decay of the velocity is observed in the shear region. This is a known feature of fully confined flows made of shape isotropic particles [3,6] and has also been observed recently in granular flows made of shape anisotropic particles [8]. Note that, for $\mathcal{R} \neq 1$, the shapes of the translational velocity profiles are nearly the same independently of \mathcal{R} , which is consistent with the experimental observations presented in Ref. [8] for spherocylindrical particles. When increasing the particle elongation, a higher slip velocity at the wall is observed in both cases, which can be reasonably associated with the lower relative dimension of the wall asperities with respect to the major axis of the particles. We recall that the bumpiness of the top and bottom walls is kept the same for all the simulations, so the ratio between particle size and asperity size increases with the aspect ratio of the particles. To gain insight into the effect of the particle elongation on the shear localization, we rescale the velocity profile by considering the localization of shear (i.e., top or bottom) and subtracting the slip contribution. This is displayed in Fig. 2(b), where $v^* = v_x/(V - v_w)$ and $z^* = z/d$ for $\mu_{pw} = 0.3$, and $v^* = (V - v_x)/(V - v_w)$ and $z^* = (L_z - z)/d$ for $\mu_{pw} = 0.05$, with v_w the slip velocity at the wall. It is clear that the decay length in the shear region is mostly unaffected by the particle shape and seems to be independent of the particles' \mathcal{R} . A slight deviation is observed for isotropic particles for the lowest value of the wall friction ($\mu_{pw} = 0.05$); however, in this case there is not a clear localization of the shear in the top region of the flow. A mild but systematic tendency of having an increase of the decay length in the creep region for larger \mathcal{R} is observed.

We display in Fig. 2(c) the granular temperature T_g profile, which is calculated as $T_g = (T_x + T_y + T_z)/3$ with $T_i = \langle (v_i - \langle v_i \rangle)^2 \rangle$, where fluctuations are computed with respect to the average velocity extrapolated at the particle center [13]. The granular temperature follows the velocity profile with higher fluctuations in the region where the shear localizes, independently of the flow pattern and the particle shape. In our flow configuration, the particle shape seems to have a negligible impact on the granular temperature profiles with only some minor differences far from the zones of shear localization.

Time-averaged angular velocity profiles are displayed in Figs. 3(a)–3(d) considering rotations with respect to the y axis, i.e., $\bar{\omega}_y$ (spinning motion), and to the z axis, i.e., $\bar{\omega}_z$ (rolling motion). We analyze these two components because they are related to the streamwise particle motion at the sidewalls (discussed below).

Figures 3(a) and 3(b) show that the mean angular velocity $\bar{\omega}_y$ systematically decreases with increasing particle elongation. For spheres in homogeneous flow conditions the angular velocity is enslaved by the flow vorticity and, on an average basis, is linked to the shear rate ($\bar{\omega}_y = -\dot{\gamma}/2$) [14–16]; hence, to understand if the shape has an effect on the inclination of a particle to rotate, in the inset of Fig. 3(a) we display the mean value, over the entire flow height, of $\bar{\omega}_y$ rescaled by the local shear rate ($10^{-4} \leq \dot{\gamma} \leq 10^{-1}$ for bottom localization and $10^{-3} \leq \dot{\gamma} \leq 10^{-1}$ for top localization, independently of \mathcal{R}). A systematic inhibition of the particle rotation is observed with increasing \mathcal{R} ($-\bar{\omega}_y/\dot{\gamma}$ is very close to 0.5 for spheres), underlining the existence of a geometrical frustration to the inclination of a particle to rotate. This behavior is consistent with the experimental results obtained in Ref. [8] and is observed independently of the flow pattern, confirming that this frustration is strongly related to the anisotropy of the particle shape. Moreover, Figs. 3(c) and 3(d) show that the frustration of particle rotations by particle shape is even stronger for rotations around the z axis (rolling component with respect to the wall). In particular, there is a marked difference between the shape isotropic and anisotropic cases. This clearly evidences that shape anisotropy hinders rolling. Note that the fact that on average motion around the z axis is damped does not mean that there are no rotations at all around that axis. In fact, it is interesting to note that the ratio of the angular velocity fluctuations $\sqrt{\langle \omega_z'^2 \rangle} = \sqrt{\langle (\omega_z - \langle \omega_z \rangle)^2 \rangle}$ to the mean angular velocity $\bar{\omega}_z$ strongly differs for shape isotropic and anisotropic particles and is increasing with \mathcal{R} [Figs. 3(e) and 3(f)].

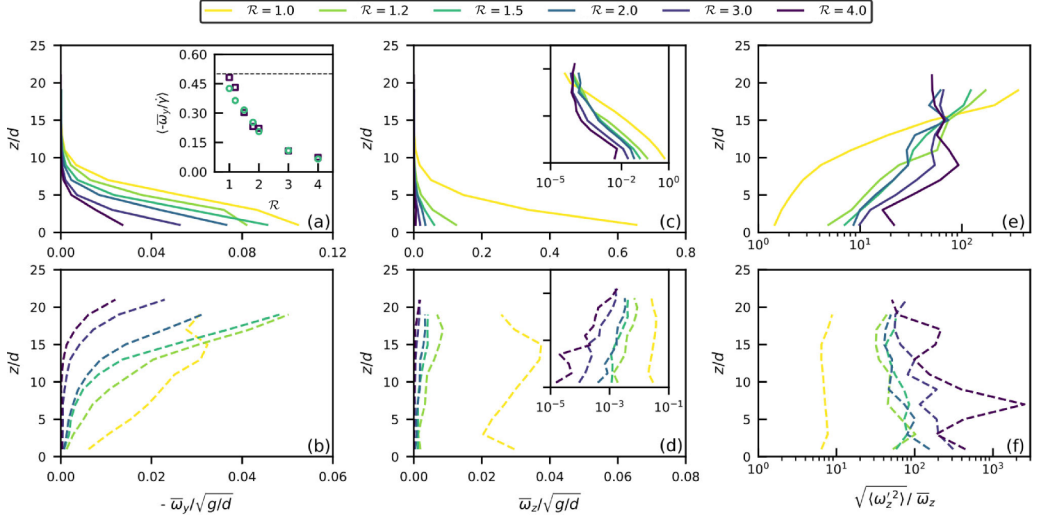


FIG. 3. Vertical profiles of (a) and (b) angular velocity $\bar{\omega}_y$, (c) and (d) angular velocity $\bar{\omega}_z$ (x axis is in logarithmic scale in the insets), and (e) and (f) ratio of angular velocity fluctuations $\sqrt{\langle \omega_z'^2 \rangle}$ over $\bar{\omega}_z$. Cases characterized by $\mu_{pw} = 0.3$ ($\mu_{pw} = 0.05$) are represented with a solid (dashed) line. The inset in (a) shows the mean angular velocity rescaled with the local shear rate $\mu_{pw} = 0.3$ (\circ) and $\mu_{pw} = 0.05$ (\square).

This suggests that isotropic particles are prone to roll on the sidewalls, while elongated particles tend to have a fluctuating rolling motion near the sidewalls.

B. Cell width L_y

In our system the interaction with the sidewalls plays a preminent role in the behavior of the granular medium. We can imagine that the farther the walls are from each other, the less of an effect they have on the system. It is therefore interesting to study the effect of the distance L_y between the walls on the flow kinematics and on wall stresses. First, we report in Figs. 4(a)–4(c) the time-averaged vertical profiles of the translational velocity v_x and of the angular velocities $\bar{\omega}_y$ and $\bar{\omega}_z$, obtained with different cell widths L_y ($=5d, 10d, 20d, 40d$), for the case of $\mathcal{R} = 2$, $\tilde{V} = 1$, $\tilde{M} = 1.2$, $\mu_{pp} = 0.3$, and $\mu_{pw} = 0.3$. Granular temperature profiles are displayed in Fig. 4(d). It is notable that the shear localization at the base of the flow fades when increasing the cell width

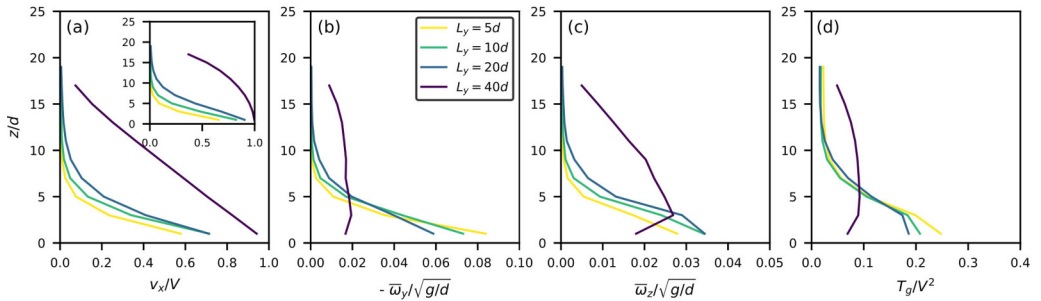


FIG. 4. Vertical profiles of (a) translational velocity v , (b) angular velocity $\bar{\omega}_y$, (c) angular velocity $\bar{\omega}_z$, and (d) granular temperature T_g for different cell widths L_y . The inset in (a) shows the translational velocity profile at the center of the cell $[(L_y - a)/2 \leq y \leq (L_y + a)/2]$. The legend in (b) applies to all figures. Profiles refer to the case of $\mathcal{R} = 2$, $\tilde{V} = 1$, $\tilde{M} = 1.2$, $\mu_{pp} = 0.3$, and $\mu_{pw} = 0.3$.

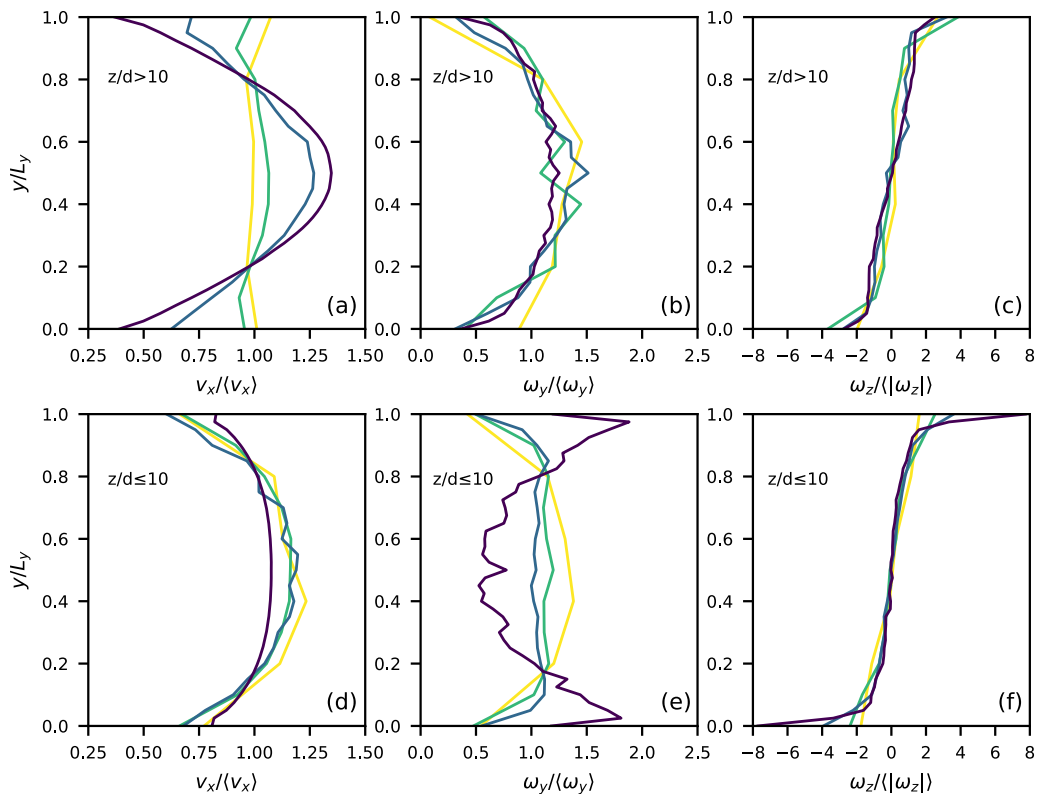


FIG. 5. Profiles, normal to the sidewalls, of (a) and (d) translational velocity v_x , (b) and (e) angular velocity ω_y , and (c) and (f) angular velocity ω_z for different cell widths L_y , for [(a)–(c)] the upper region of the flow ($z > 10d$) and [(d)–(f)] the bottom region of the flow ($z \leq 10d$). Profiles refer to the case of $\mathcal{R} = 2$, $\tilde{V} = 1$, $\tilde{M} = 1.2$, $\mu_{pp} = 0.3$, and $\mu_{pw} = 0.3$. The meaning of colors is the same as in Fig. 4(b).

[see Fig. 4(a)]. For the case $L_y = 40d$, at the sidewalls we observe an almost linear velocity profile, while in the center of the cell the shear tends to localize in the top region of the flow [see the inset in Fig. 4(a)]. Based on the different flow regimes observed in Fig. 4(a), it seems evident that increasing the wall separation reduces the importance of wall friction with respect to bulk friction and this favors a velocity profile with top localization. We therefore expect to observe a shear top localization also at the sidewalls for large cells. For narrower cells instead the shear localization is always observed in the bottom region of the flow without significant differences moving from the sidewalls to the center of the cell. The modification of the flow pattern reflects also on the angular velocity profiles with the case $L_y = 40d$ that strongly differs from the others. In this case we observe an almost constant value of the angular (spinning) velocity $\bar{\omega}_y$ [Fig. 4(b)] and a linear decrease of the angular (rolling) velocity $\bar{\omega}_z$ with the flow height [Fig. 4(c)]. Granular temperature profiles [Fig. 4(d)] follow the velocity ones with higher fluctuations in the region where the shear localizes (cases with $L_y = 5d, 10d, 20d$), while for the case $L_y = 40d$, for which $\dot{\gamma}$ is approximately the same over the entire flow height, we observe an almost constant value of T_g .

In order to understand the effect of lateral walls it is also evidently interesting to study the transverse profiles of the kinematic variables. Normal to the sidewall profiles of the relative translational and angular velocities are displayed in Fig. 5. It should be pointed out that we display quantities rescaled on their averaged value in the y direction. These are reported with reference to the bottom region $z \leq 10d$ [Figs. 5(d)–5(f)] and to the top region of the flow $z > 10d$ [Figs. 5(a)–5(c)] due to the possible heterogeneity along the flow height.

We note that variations of the relative velocity $v_x/\langle v_x \rangle$ are much more pronounced in the bottom region for the cases characterized by a shear localization at the base of the flow [see Fig. 5(d)]. This is consistent with previous results on spherical particles [6]. For the case $L_y = 40d$, in which the shear rate is almost constant along the flow height, the opposite behavior is observed with the most important variations of the relative velocity (up to 60%) in the upper region of the flow [see Fig. 5(a)].

We also observe an interesting difference in the normal to the sidewall profile of the relative spinning velocity $\omega_y/\langle \omega_y \rangle$ in the bottom region of the flow. This has an opposite trend whether or not shear localizes [see Fig. 5(e)]. In the former case ω_y is maximum (and almost constant) in the bulk region and minimum at sidewalls, while in the latter case ω_y is minimum in the bulk and progressively increases moving towards the sidewalls. This behavior is due to the fact that when bottom localization is not observed (case $L_y = 40d$) the shear rate is higher near the sidewalls than in the center of the cell in the bottom region of the flow, while when the flow localizes the shear rate is larger in the bulk of the material along the entire flow height. In the upper region of the system no significant differences are observed when changing the cell width [see Fig. 5(b)] and ω_y is always higher in the bulk region. The profiles of the relative rolling velocity $\omega_z/\langle \omega_z \rangle$ present, globally, a linear variation in the y direction. In the bottom region of the flow, the interactions with the sidewalls have a mild effect on the rolling motion of the particles when shear localization is observed (cases with $L_y \leq 20d$), while a very sharp variation of the rolling velocity is observed in the case in which the flow is not localized (case with $L_y = 40d$), as displayed in Fig. 5(f).

The results presented in this section show that, by changing the particles' aspect ratio, the particle-wall friction coefficient, and the distance between the sidewalls, the confined flow geometry displays a variety of flow profiles. In the following we will see how these flow patterns influence the effective friction at sidewalls.

IV. EFFECTIVE WALL FRICTION

In this section we characterize the effective friction between the streaming particles and the lateral walls. We estimate the streamwise effective friction at the wall by computing the ratio of the average force in the flow direction to the average force in the direction normal to the sidewalls, i.e., $\mu_w^x = \langle F_x \rangle / \langle F_y \rangle$ [3], exchanged between the particles and the sidewalls. Similarly, we estimate the transverse (vertical) friction coefficient as $\mu_w^z = \langle F_z \rangle / \langle F_y \rangle$. We first discuss how wall friction mobilization is affected by the particle shape and by the cell width. Then we present an alternative scaling law for the streamwise wall friction, which takes into account the local kinematics close to the wall. Finally, we test the scaling law in a gravity-driven flow configuration.

A. Particle shape: Aspect ratio \mathcal{R}

Profiles of μ_w^x are shown in Figs. 6(a) and 6(b) for different aspect ratios. Similarly to previous results on spherical particles [3,5,6,10], the streamwise effective wall friction displays a different behavior according to the flow pattern. When the shear localizes at the bottom, the wall friction is only partially mobilized ($\mu_w^x < \mu_{pw}$) in the flow direction. The effective friction μ_w^x is higher in the shear region and it decreases systematically with z . This degradation of the wall friction is consistent with experimental observations [5,9]. In contrast, when top localization is observed μ_w^x is minimum in the shear region; then it rapidly increases and a nearly full mobilization of wall friction is observed in the bottom zone of the flow ($\mu_w^x \approx \mu_{pw}$), which moves as a plug.

Interestingly, we observe that the streamwise effective wall friction is also affected by the shape anisotropy of the particles. The lowest values of μ_w^x are obtained for isotropic particles and a systematic increase of μ_w^x with \mathcal{R} is observed, independently of the flow pattern. Referring to the case of bottom localization [Fig. 6(a)], the larger differences are observed for low \mathcal{R} : The effective friction μ_w^x increases in the range $1 \leq \mathcal{R} \leq 2$ and then it seems to saturate for $\mathcal{R} > 2$. A similar

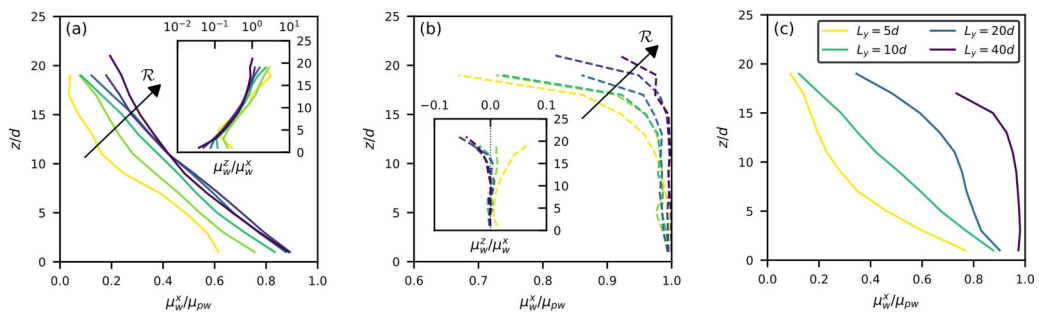


FIG. 6. Vertical profiles of the streamwise effective wall friction μ_w^x for (a) $\mu_{pw} = 0.3$ (shear is localized at the bottom) and (b) $\mu_{pw} = 0.05$ (shear is localized at the top) for different aspect ratios \mathcal{R} . (c) Profiles of the streamwise effective wall friction μ_w^x with $\mathcal{R} = 2$ for different cell widths L_y (shear is localized at the bottom for $L_y \leq 20d$ and is almost uniform along the flow height for the case $L_y = 40d$). Effective friction μ_w is rescaled on the particle-wall friction coefficient μ_{pw} . The insets in (a) and (b) show vertical profiles of the ratio of the transverse effective friction over the streamwise effective friction μ_w^z / μ_w^x . The meaning of colors in (a) and (b) is the same as in Fig. 3.

behavior is observed when shear localizes at the top of the flow [Fig. 6(b)] but with a marked difference also for the larger \mathcal{R} .

We note that the transverse wall friction μ_w^z [see the insets in Figs. 6(a) and 6(b)] is nearly always smaller than the streamwise one. This is because the medium is globally characterized by a dominant horizontal flow. The only exception is observed in creeplike regions, i.e., the upper region of the flow when shear localizes at the bottom [see the inset in Fig. 6(a)], where μ_w^z becomes of the same order and even larger than μ_w^x . The equivalence of streamwise and transverse wall friction in creep zones was already observed for isotropic particles, both experimentally and numerically [4,5]. In fact, in these regions the particles' motion is characterized by a transverse (vertical) fluctuating motion rather than by a streamwise one ($T_z > T_x$, result not shown here). We observe a higher ratio μ_w^z / μ_w^x for shorter particles, which is mainly due to the higher mobilization of the streamwise wall friction for longer particles (for $\mathcal{R} \neq 1$ the transverse wall friction μ_w^z is nearly the same for all cases).

Always concerning μ_w^z , an interesting difference is observed in the upper region of the flow when shear localizes at the top. Even if the transverse friction is only slightly mobilized, we note that the sidewalls seem to act in an opposite way for shape isotropic and anisotropic particles. For the former the sidewalls exert, on average, a downward force on the grains, while for the latter the sidewalls tend to sustain the medium. This small but systematic effect could be due to some secondary motion (e.g., convective rolls) superposed on the shear flow and coupling to the rotational dynamics of the grains. The behavior of wall friction in the presence of secondary flows is an interesting subject which we leave for future study.

B. Cell width L_y

In order to study the influence of the cell width L_y on the streamwise wall friction, we present in Fig. 6(c) the vertical profiles of μ_w^x for different cell widths. Interestingly, we observe a systematic higher mobilization of the effective wall friction when increasing the width L_y of the cell. For the narrower cells ($L_y = 5d, 10d$), μ_w^x has a maximum at the base of the flow, where shear localizes, and progressively decreases with z . A further increase of cell width ($L_y = 20d$) determines a significant increase and an almost constant value of the mobilized friction in the bottom region of the flow (shear region), while a strong degradation of μ_w^x with z is still observed in the top (creeplike) region. Finally, for the largest cell ($L_y = 40d$) the effective friction is almost completely mobilized in the bottom region ($\mu_w^x \approx \mu_{pw}$) and shows only a mild degradation in the top region of the flow. It is notable that the effect of increasing the width of the cell acts in the same direction as a decreasing of the particle-wall friction coefficient. The increase of friction mobilization with L_y is evidently

related to the progressive reduction of the slowly (creeplike) moving zone, which disappears for the case $L_y = 40d$ and leads to the development of a nearly linear velocity profile. This is further proof that wall friction weakening is maximum in slowly (creeplike) moving zones.

C. Streamwise effective wall friction scaling

From the preceding text it is evident that the effective wall friction has a nontrivial behavior and we observe a dependence on both the flow pattern and the particle shape. Our geometry is therefore a good benchmark for boundary conditions because flow profiles change significantly when varying parameters such as the particle-wall friction coefficient and the distance between the sidewalls. In what follows, we propose and discuss a scaling law for streamwise wall friction based on the kinematic properties of the particles. Recent works have related the degradation of wall friction to translational velocity fluctuations or particle rotation [3,6,7,9,10]. The scaling laws proposed in those works have shown, to a certain extent, fair agreement with the data but have been applied for the case of spherical particles only. We tested these scalings and found that, though qualitatively describing wall friction weakening also for elongated particles, they fail to correctly describe the different mobilization of the effective wall friction with particle shape.

Due to the effect of particle shape on the frustration of particle rotations (see Fig. 3) and considering that the effective wall friction also seems to depend on particle anisotropy, it is tempting to associate the mobilization of wall friction with a balance between slip velocity and rolling motion. It should be noted that spinning motion may also cause a degradation of wall effective friction. Nevertheless, in our system $v_x \gg \bar{\omega}_y a$; hence we assume that the effect of particle spinning motion on μ_w^x can be neglected [17]. On the other hand, we have seen that the rolling component of the angular velocity may be characterized by strong fluctuations. Therefore, we introduce here a scaling parameter for effective wall slip that is based on the average kinetic energy of the rolling motion, $\kappa = v_x/a\sqrt{\langle\omega_z^2\rangle}$, where ω_z is the instantaneous (rolling) angular velocity. We recall that we refer to average quantities at the sidewalls since we focus on the interaction behavior of the granular medium with such flat interfaces. Figure 7(a) displays the rescaled effective friction coefficient μ_w^x/μ_{pw} as a function of the parameter κ . The scaling performs well for several orders of magnitude and over a large range of particle aspect ratios. For the intermediate case of $\mathcal{R} = 2$, we display also data obtained in a wider range of parameters: $\mu_{pp} = 0.1-1$ (\triangleleft), $\mu_{pw} = 0.05-0.3$ (\triangle), $\bar{M} = 0.2-4.8$ (∇), $\bar{V} = 1-10$ (\triangleright), and $L_y = 5-40$ (\diamond). The scaling seems therefore very robust since it is also independent of the driving velocity, the applied pressure, the width of the channel, and the wall-particle and particle-particle frictional properties.

In order to gain insight into this scaling law it is useful to first describe qualitatively the behavior of the effective friction as a function of the scaling parameter κ . The parameter κ permits identification of three particle kinematic regimes which directly link to the mobilized friction: two limit regimes, i.e., a no-slip–pure rolling regime, for $\kappa \leq 0.1$ (i.e., $v_x \ll a\sqrt{\langle\omega_z^2\rangle}$), in which the effective wall friction is negligible ($\mu_w^x \approx 0$), and a pure sliding regime, for $\kappa \geq 10$ (i.e., $v_x \gg a\sqrt{\langle\omega_z^2\rangle}$), in which the effective friction is almost completely mobilized ($\mu_w^x \approx \mu_{pw}$), and a third, intermediate regime encountered for $0.1 < \kappa < 10$. In this regime neither of the two mentioned mechanisms is dominant, sliding and rolling motion coexist, and the wall friction is mobilized according to the relative magnitude of these two contributions ($0 < \mu_w^x/\mu_{pw} < 1$). We observe a remarkable variation of μ_w^x for relatively small variations of the parameter κ , which indicates a strong coupling between sliding and rolling motion in this intermediate regime. Finally, the introduction of the characteristic length a in the scaling parameter κ makes the data collapse on a master curve. Nevertheless, the effect of particle shape is reasonably also hidden in ω_z .

To explain why this scaling describes so well the effective wall friction behavior for a large range of particle elongations, we decompose the instantaneous angular velocity ω_z into a mean ($\bar{\omega}_z$) and a fluctuating (ω_z') component. The former is an average rolling motion with a given rotation direction that in our flow configuration may be related to the existence of a slight velocity gradient normal to the wall, i.e., $\partial v_x/\partial y$. The latter accounts for an intermittent fluctuating rolling motion of the

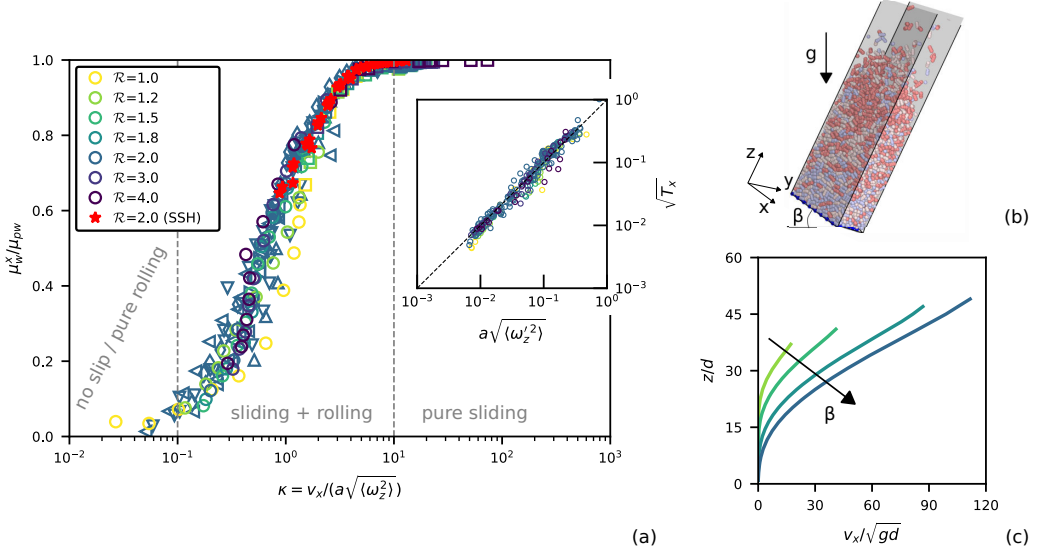


FIG. 7. (a) Rescaled effective friction coefficient at the wall versus the parameter $\kappa = v_x/a\sqrt{\langle\omega_z^2\rangle}$ (for $\tilde{V} = 1$, $\tilde{M} = 1.2$, and $\mu_{pp} = 0.3$): $\mu_{pw} = 0.3$ (\circ) and $\mu_{pw} = 0.05$ (\square). Different colors correspond to different values of \mathcal{R} . For $\mathcal{R} = 2$ the symbols represent variation of several parameters, demonstrating the robustness of the scaling: $\mu_{pp} = 0.1$ – 1 (\triangleleft), $\mu_{pw} = 0.075$ – 0.2 (\triangle), $\tilde{M} = 0.2$ – 4.8 (∇), $\tilde{V} = 1$ – 10 (\triangleright), and $L_y = 5d$ – $40d$ (\diamond). Star markers correspond to data obtained from gravity-driven flow simulation (see the text for details) at different angles β of the inclined plane. (b) Typical geometry of the gravity-driven flow simulation. (c) Translational velocity profiles obtained in the gravity-driven flow configuration ($\beta = 42^\circ, 47^\circ, 52^\circ, 55^\circ$). The inset in (a) shows that the fluctuating rolling motion globally scales with the square root of the streamwise velocity fluctuations.

particles. We observe that this fluctuating motion globally scales with the square root of the streamwise velocity fluctuations [inset in Fig. 7(a)] and may be associated with the particles' agitation. This fluctuating component is dominant for sufficiently elongated particles (i.e., $\mathcal{R} \geq 2$), while for almost isotropic particles the average rolling motion is also contributing to the degradation of a pure sliding regime at the wall. The observed scaling of wall friction with the parameter κ involving the average rolling kinetic energy can be seen as comprising and unifying the previous ones [3,6,7], because it takes into account the average rolling motion as well as the fluctuating motion.

With particular regard to the scaling proposed in Ref. [3] and based on the root mean square of the streamwise velocity fluctuations, given that $\sqrt{T_x} \propto a\sqrt{\langle\omega_z^2\rangle}$ and since $\sqrt{\langle\omega_z^2\rangle}$ is generally larger than $\bar{\omega}_z$ in our flows [see Figs. 3(e) and 3(f)] means that, for a given particle shape, the effective wall friction scales, globally, with the slip parameter $v_x/\sqrt{T_x}$. However, the scaling based on $v_x/\sqrt{T_x}$ does not rescale well data from different aspect ratios. Deviations from a master curve are observed especially in the zone for which sliding and rolling motion are correlated. The best collapse to a master curve is therefore obtained with the parameter κ discussed above.

In order to test the generality of the proposed scaling law, we also perform numerical simulations in a free-surface gravity-driven flow configuration. The cell [see Fig. 7(b)] has the same dimension as the one used for the confined flow in the x and y directions ($L_x = 20a$ and $L_y = 10d$). The same bottom wall as in the confined configuration is used, while the flow is not bounded at the top. An intermediate aspect ratio $\mathcal{R} = 2$ is considered and the granular sample is composed of 3200 particles. The contact parameters are the same as those used in the confined flow simulations (see Sec. II). The angle between the horizontal and the main flow direction β is set to a high value at first ($\beta = 60^\circ$) and then is reduced to the desired value. This initial condition permits the material to lose memory of the initial structure. This flow configuration leads to the so-called superstable

heap (SSH) regime [1,6,18–20]. In this type of flow, both stresses and shear rate vary with z . The inertial number $I(z) = \dot{\gamma}d/\sqrt{p/\rho}$, with $\dot{\gamma}(z) = \partial v_x/\partial z$, ρ the mass density of the system, and p the local pressure, a dimensionless number commonly used to characterize granular flow regimes, is thus not uniform. We compute the effective wall friction coefficient only in the zones corresponding to a dense flow, i.e., $10^{-4} < I(z) < 10^{-1}$, disregarding the stable heap beneath and the grains in the collisional regime above [velocity profiles are displayed in Fig. 7(c)]. Note that the confined shear flows presented in the paper have a typical range $10^{-4} \leq I(z) \leq 10^{-2}$, which corresponds to dense slow flows. The data from the SSH configuration collapse on the same master curve obtained for the confined flows [star markers in Fig. 7(a)], showing that our scaling well describes the wall friction mobilization in a totally different flow configuration. As a last comment, we note that the relation between effective wall friction and dilatancy has often been neglected in the literature. In our stress-controlled system, the solid volume fraction is not homogeneous and its average value depends on system parameters such as the vertical confinement. While we do not address this in detail here, the fact that the scaling law is verified in both the confined and the free-surface configurations seems to suggest that the dilatancy does not play a major role in the effective wall friction scaling.

V. CONCLUSION

In this work we have discussed, by means of discrete numerical simulations, the kinematics and the wall stresses in a 3D, dense, fully confined granular flow of anisotropic particles. We have shown that a variety of kinematic profiles can be obtained when varying the particle-wall friction coefficient and the distance between the sidewalls. In our peculiar flow configuration, the effect of particle shape affects mainly the angular velocity profiles: As one may expect, both spinning and rolling motions are frustrated. On the other hand, apart from the effect of the different relative bumpiness on the slip velocity at bumpy walls, the translational velocity and granular temperature profiles are similar between different particle elongations. Particle elongation also affects the wall stresses, which we have studied through the concept of effective wall friction. In particular, elongated particles show less friction weakening at the wall than more isotropic particles. Due to its rich flow and stress profiles, our flow configuration is an ideal benchmark for boundary conditions. Combining wall stress and kinematics data, we have shown that in dense granular flows the effective friction at flat interfaces scales according to a balance between sliding and angular motion of the particles. We have proposed a scaling law for 3D bounded granular flows based on the average kinetic energy of the rolling motion, which relates the particle kinematics regime to the friction mobilization. Three regimes have been identified: pure sliding ($\mu_w^x \approx \mu_{pw}$), no-slip–pure rolling ($\mu_w^x \approx 0$), and sliding and rolling coupling ($0 < \mu_w^x/\mu_{pw} < 1$). This description is relevant both for shape isotropic and elongated particles and in different flow configurations (i.e., shear driven and gravity driven). The proposed scaling law unifies the previous frameworks associating wall friction degradation with particle agitation [3,6] and with absolute particle rotation [7]. The former can in fact be associated with the fluctuating angular motion of the grains, while the latter is straightforwardly related to the root mean square of the rolling velocity.

The results reported here advance our understanding of the friction mobilization at flat interfaces, providing evidence that particle shape affects effective wall friction via the angular dynamics. This is particularly meaningful for the application of rheological laws to real materials, which are often composed of anisotropic particles, and may revive the debate about the relevant variables to be included in high-order continuum modeling of dense granular flows, with a point in favor of particle rotations. It would also be interesting to understand the effect of more complex contact models (e.g., static or dynamic friction and cohesion) on the proposed scaling. It should be noted that the scaling has been defined for sidewall friction, i.e., the wall in the direction parallel to gravity. In the future, the universality of the proposed scaling and of the associated mechanisms should be tested in other flow configurations, with a primary objective to understand if it may apply also for basal friction [21,22].

ACKNOWLEDGMENTS

The authors acknowledge financial support from ANR (Grant No. ANR-20-CE08-0028 MoNo-CoCo). This work was supported by the GLiCID High Performance Computing facility.

-
- [1] N. Taberlet, P. Richard, A. Valance, W. Losert, J. M. Pasini, J. T. Jenkins, and R. Delannay, Superstable Granular Heap in a Thin Channel, *Phys. Rev. Lett.* **91**, 264301 (2003).
 - [2] P. Jop, Y. Forterre, and O. Pouliquen, Crucial role of sidewalls in granular surface flows: Consequences for the rheology, *J. Fluid Mech.* **541**, 167 (2005).
 - [3] R. Artoni and P. Richard, Effective Wall Friction in Wall-Bounded 3D Dense Granular Flows, *Phys. Rev. Lett.* **115**, 158001 (2015).
 - [4] P. Richard, A. Valance, J.-F. Métayer, P. Sanchez, J. Crassous, M. Louge, and R. Delannay, Rheology of Confined Granular Flows: Scale Invariance, Glass Transition, and Friction Weakening, *Phys. Rev. Lett.* **101**, 248002 (2008).
 - [5] R. Artoni, A. Soligo, J.-M. Paul, and P. Richard, Shear localization and wall friction in confined dense granular flows, *J. Fluid Mech.* **849**, 395 (2018).
 - [6] P. Richard, R. Artoni, A. Valance, and R. Delannay, Influence of lateral confinement on granular flows: Comparison between shear-driven and gravity-driven flows, *Granul. Matter* **22**, 81 (2020).
 - [7] F.-L. Yang and Y.-T. Huang, New aspects for friction coefficients of finite granular avalanche down a flat narrow reservoir, *Granul. Matter* **18**, 1 (2016).
 - [8] A. Pol, R. Artoni, P. Richard, P. R. N. da Conceição, and F. Gabrieli, Kinematics and shear-induced alignment in confined granular flows of elongated particles, *New J. Phys.* **24**, 073018 (2022).
 - [9] C.-C. Lin, R. Artoni, F.-L. Yang, and P. Richard, Influence of granular temperature and grain rotation on the wall friction coefficient in confined shear granular flows, *EPJ Web Conf.* **249**, 03026 (2021).
 - [10] C.-C. Lin, R. Artoni, F. L. Yang, and P. Richard, Modeling wall friction coefficient for a simple shear granular flow in view of the degradation mechanism, *J. Fluid Mech.* (to be published).
 - [11] C. Kloss, C. Goniva, A. Hager, S. Amberger, and S. Pirker, Models, algorithms and validation for opensource DEM and CFD-DEM, *Prog. Comput. Fluid Dyn.* **12**, 140 (2012).
 - [12] T. Börzsönyi, B. Szabó, S. Wegner, K. Harth, J. Török, E. Somfai, T. Bien, and R. Stannarius, Shear-induced alignment and dynamics of elongated granular particles, *Phys. Rev. E* **86**, 051304 (2012).
 - [13] R. Artoni and P. Richard, Average balance equations, scale dependence, and energy cascade for granular materials, *Phys. Rev. E* **91**, 032202 (2015).
 - [14] M. Prochnow, *Ecoulements denses de grains secs*, Ph.D. thesis, Ecole des Ponts ParisTech, 2012.
 - [15] F. da Cruz, S. Emam, M. Prochnow, J.-N. Roux, and F. Chevoir, Rheophysics of dense granular materials: Discrete simulation of plane shear flows, *Phys. Rev. E* **72**, 021309 (2005).
 - [16] G. Koval, J.-N. Roux, A. Corfdir, and F. Chevoir, Annular shear of cohesionless granular materials: From the inertial to quasistatic regime, *Phys. Rev. E* **79**, 021306 (2009).
 - [17] Z. Farkas, G. Bartels, T. Unger, and D. E. Wolf, Frictional Coupling between Sliding and Spinning Motion, *Phys. Rev. Lett.* **90**, 248302 (2003).
 - [18] N. Taberlet, P. Richard, E. Henry, and R. Delannay, The growth of a super stable heap: An experimental and numerical study, *Europhys. Lett.* **68**, 515 (2004).
 - [19] W. Bi, R. Delannay, P. Richard, N. Taberlet, and A. Valance, Two- and three-dimensional confined granular chute flows: experimental and numerical results, *J. Phys.: Condens. Matter* **17**, S2457 (2005).
 - [20] W. Bi, R. Delannay, P. Richard, and A. Valance, Experimental study of two-dimensional, monodisperse, frictional-collisional granular flows down an inclined chute, *Phys. Fluids* **18**, 123302 (2006).
 - [21] R. Artoni, A. C. Santomaso, M. Go', and P. Canu, Scaling Laws for the Slip Velocity in Dense Granular Flows, *Phys. Rev. Lett.* **108**, 238002 (2012).
 - [22] O. Roche, S. van den Wildenberg, A. Valance, R. Delannay, A. Mangeney, L. Corna, and T. Latchimy, Experimental assessment of the effective friction at the base of granular chute flows on a smooth incline, *Phys. Rev. E* **103**, 042905 (2021).